China Instrument and Control Society
Instrumentation
OPEN ACCESS
INSTRUMENTATION, Vol. 13, No. 3, September 2026 https://doi.org/10.15878/j.instr.202600400

Pipeline Inspection

Full-Waveform Inversion Imaging of Defects Using Guided Waves from a Magnetostrictive Patch Transducer with a Perpendicular Static Magnetic Field

Jing Wang, Shujuan Wang, Zhichao Li*

[1] School of Electrical Engineering and Automation, Harbin Institute of Technology, Harbin, Heilongjiang 150001, China

* Corresponding author email: zhichao.li@hit.edu.cn

Abstract: Conventional magnetostrictive patch transducers can suffer from a non-uniform static magnetic field and limited transduction efficiency in ultrasonic guided-wave testing. This study presents a transducer with a perpendicular static magnetic field and combines it with full-waveform inversion for guided-wave imaging of defects in plates and pipes. An equivalent surface-stress model was established for the proposed structure and validated by finite-element simulation. Guided-wave experiments were then used to determine how the static magnetic field affected signal amplitude and to compare the proposed design with other magnetostrictive patch transducers. Finally, transducer arrays acquired defect signals for full-waveform inversion imaging. The transducer effectively generated shear-horizontal guided waves. Signal amplitude reached its maximum at a surface magnetic flux density of approximately 70 mT and was about twice that obtained with a horizontal-field transducer based on the inverse Wiedemann effect. The plate-defect contours were clearly reconstructed, with maximum depth errors below 5.0%. Pipe imaging recovered the principal defect locations and contours. The proposed transducer therefore provides signals suitable for guided-wave full-waveform inversion imaging.

Keywords: magnetostrictive patch transducer; perpendicular static magnetic field; ultrasonic guided waves; full-waveform inversion; defect imaging

Copyright: © 2026 by the authors. This article is licensed under a Creative Commons Attribution 4.0 International License (CC BY) license (https://creativecommons.org/licenses/by/4.0/).

Citation: Jing Wang, Shujuan Wang, Zhichao Li. "Full-Waveform Inversion Imaging of Defects Using Guided Waves from a Magnetostrictive Patch Transducer with a Perpendicular Static Magnetic Field." Instrumentation 13, no.3 (September 2026). https://doi.org/10.15878/j.instr.202600400

1 Introduction

Metal plates and pipes are widely used in petrochemical processing, energy transport, machinery and aerospace engineering. During long-term service, corrosion, fatigue, erosion and external loading can produce local wall thinning, holes and cracks, creating risks of leakage and fracture. Efficient and reliable non-destructive testing and defect-imaging techniques are therefore essential for the safe operation of industrial equipment[1,2].

Ultrasonic guided waves propagate over long distances, cover large areas and support efficient inspection. They are therefore well suited to large-scale testing of thin-walled structures such as plates and pipes[3-5]. However, the reliability of guided-wave inspection depends strongly on the excitation and reception performance of the transducer. Low excitation efficiency, weak signal amplitude or poorly defined modes directly compromise subsequent signal analysis and defect imaging.

Magnetostrictive patch transducers generate and receive guided waves through electromagnetic coupling. They require no liquid couplant, have flexible

configurations, support array deployment and can readily excite shear-horizontal and torsional guided waves. These characteristics make them attractive for plate and pipe inspection [6-8]. Most existing designs use a horizontal or circumferential static magnetic field. Previous studies have improved guided-wave excitation through permanent-magnet configurations, coil design, magnetic-circuit optimisation and auxiliary soft-magnetic materials[9-14]. In large plates or large-diameter pipes, however, greater spacing between adjacent permanent magnets can weaken the static field and make it non-uniform, thereby reducing transduction efficiency. Bias-field uniformity is an important determinant of transducer output[15]. Further optimisation of the way in which the static field is applied therefore remains valuable.

As non-destructive testing progresses from defect localisation to shape reconstruction and quantitative sizing, echo amplitude, arrival time or any single signal feature is no longer sufficient for high-precision assessment. Conventional scanning, phased-array, time-reversal and tomographic methods have been applied in various settings[16-21]. Their resolution and angular coverage can nevertheless be limited, and artefacts may arise for complex defects or restricted arrays. Full-waveform inversion uses the amplitude, phase and travel-time information in guided-wave signals to reconstruct material parameters or thickness distributions within a defective region. It therefore provides an effective means of assessing defect contours[22-24]. Recent applications include corrosion imaging in plates, defect detection in complex structures and multiparameter ultrasonic tomography[25-30].

Here, we propose a magnetostrictive patch transducer with a perpendicular static magnetic field and combine it with full-waveform inversion for guided-wave defect imaging. The main contributions are fourfold. First, the perpendicular static-field configuration allows the magnetising face to act directly on the magnetostrictive region and provides a compact structure suitable for array deployment. Second, an equivalent surface-stress model is established and validated using finite-element analysis. Third, the magnetostrictive and Lorentz-force surface stresses are quantitatively compared, identifying magnetostriction as the dominant transduction mechanism. Finally, the proposed transducer is combined with full-waveform inversion and evaluated through finite-element analyses of array configuration and defect geometry, followed by experimental validation of wall-thinning defects in plate and pipe specimens.

2 Materials and Methods

2.1 Design of the Magnetostrictive Patch Transducer with a Perpendicular Static Magnetic Field

A conventional magnetostrictive patch transducer with a horizontal static magnetic field generally comprises the specimen, coil, magnetostrictive patch and permanent magnets, as shown in Fig. 1a. The permanent magnets provide a horizontal static field in the patch, whereas an alternating current in the coil generates a dynamic field. Their coupled action produces periodic deformation of the patch and excites guided waves in the specimen. Transduction performance depends strongly on magnetic-field strength and uniformity[9-15]. For a large specimen or a structure with appreciable curvature, increased magnet spacing can weaken the field and make its distribution non-uniform, thereby reducing transduction efficiency.

To address this limitation, we designed the transducer shown in Fig. 1b. The magnet is positioned above the coil, so the static field acts through the thickness of the magnetostrictive region. Compared with a horizontal-field configuration, this arrangement applies the magnetising face more directly to the patch and reduces field attenuation caused by changes in magnet spacing. It also produces a compact transducer that is suitable for array deployment and inspection of curved structures.

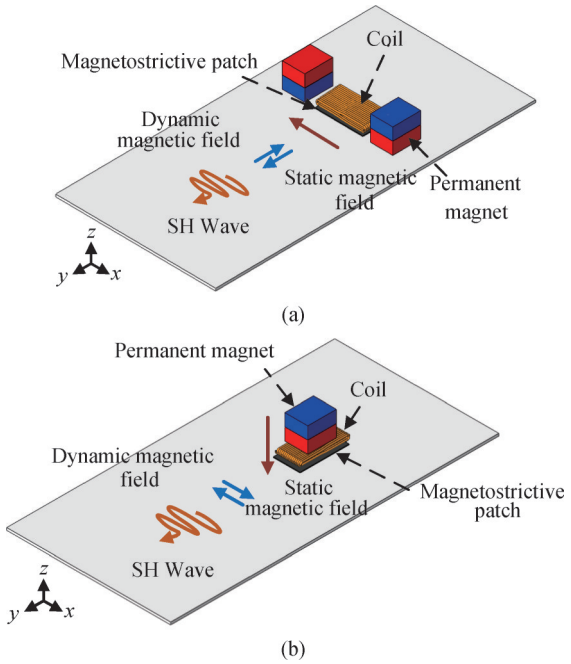


Fig.1 Schematics and operating principles of magnetostrictive patch transducers with different static-field orientations: (a)Horizontal static-field transducer; (b)Perpendicular static-field transducer.

2.2 Guided-Wave Excitation Model and Finite-Element Validation

To examine the guided-wave excitation mechanism of the proposed transducer, we established an analytical model of its equivalent surface stress. The magnet supplies a perpendicular static field in the z direction. The coil extends along y, and its current generates dynamic-field components along x and z. The static and dynamic fields jointly act on the patch to produce x-directed strain,

thereby generating shear-horizontal guided waves that propagate along *y*. For tractability, the static field was assumed to be approximately uniform within the transduction region. The magnetostrictive patch was treated as homogeneous and isotropic, and displacement current and magnetostrictive volume change were neglected. According to magnetostriction, the dynamic field $\tilde{\boldsymbol{H}}$ induces the strain $\boldsymbol{S}^{(\mathrm{MS})}$, given by:

$$\boldsymbol{S}^{(\mathrm{MS})}=\boldsymbol{d}^{(\mathrm{MS})}\tilde{\boldsymbol{H}} \tag{1}$$

where $\tilde{\boldsymbol{H}}$ is the dynamic magnetic-field strength (A/m), and $\boldsymbol{d}^{(\mathrm{MS})}$ is the effective piezomagnetic coefficient associated with the static field.

When the static magnetic field is directed along *z*, the piezomagnetic coefficient matrix is

$$\boldsymbol{d}^{(\mathrm{MS})}=\begin{bmatrix} 0 & 0 & 0 & 0 & \dfrac{3\varepsilon_{\bar{H}_z}}{\bar{H}_z} & 0 \\ 0 & 0 & 0 & \dfrac{3\varepsilon_{\bar{H}_z}}{\bar{H}_z} & 0 & 0 \\ -\dfrac{\gamma_{\bar{H}_z}}{2} & -\dfrac{\gamma_{\bar{H}_z}}{2} & \gamma_{\bar{H}_z} & 0 & 0 & 0 \end{bmatrix}^{\mathrm{T}} \tag{2}$$

where *x*, *y*, and *z* denote the Cartesian coordinate directions; $\bar{H}_z$is the *z*-directed static magnetic-field strength (A/m); $\varepsilon_{\bar{H}_z}$is the magnetostrictive strain along the static-field direction at $\bar{H}_z$; $\gamma_{\bar{H}_z}$ is the slope of the magnetostriction curve under the static field $\bar{H}_z$.

The dynamic magnetic field $\tilde{\boldsymbol{H}}$can be expressed as:

$$\tilde{\boldsymbol{H}}=\left(\tilde{H}_x,\tilde{H}_y,\tilde{H}_z\right) \tag{3}$$

where$\tilde{H}_x$, $\tilde{H}_y$, and $\tilde{H}_z$ are the *x*, *y* and *z* components of the dynamic magnetic field. Because of the coil geometry and current direction, $\tilde{H}_y$can be neglected in the present model.

Substituting the piezomagnetic coefficient matrix and the dynamic-field expression into the magnetostrictive strain relation, with the material stiffness matrix defined as

$$\begin{bmatrix} c_{11} & c_{12} & c_{12} & & & \\ c_{12} & c_{11} & c_{12} & & & \\ c_{12} & c_{12} & c_{11} & & & \\ & & & c_{44} & & \\ & & & & c_{44} & \\ & & & & & c_{44} \end{bmatrix} \tag{4}$$

$$c_{11}=\lambda+2\mu,\ c_{12}=\lambda,\ c_{44}=\mu \tag{5}$$

where μ and λ are the Lame constants.

The magnetostrictive stress $\boldsymbol{\sigma}^{(\mathrm{MS})}$ is therefore

$$\boldsymbol{\sigma}^{(\mathrm{MS})}=\begin{bmatrix} c_{11} & c_{12} & c_{12} & & & \\ c_{12} & c_{11} & c_{12} & & & \\ c_{12} & c_{12} & c_{11} & & & \\ & & & c_{44} & & \\ & & & & c_{44} & \\ & & & & & c_{44} \end{bmatrix}\boldsymbol{S}^{(\mathrm{MS})} \tag{6}$$

The equivalent surface stress associated with the converted magnetostrictive body force is superposed on the surface stress generated directly by magnetostriction. Because the *x*-directed magnetostrictive surface stress is the main source of shear-horizontal guided waves, it is considered here$\sigma_x^{(\mathrm{MS,e})}$. The simplified relation from the original model gives:

$$\sigma_x^{(\mathrm{MS,e})}=-\frac{6\mu\varepsilon_{\bar{H}_z}}{\bar{H}_z}\sum_{n=0}^{\infty}q_n\odot_n\cos\left(k_nx\right)+\mu\gamma_{\bar{H}_z}\sum_{n=0}^{\infty}\frac{k_n^2}{q_n}\odot_n\cos\left(k_nx\right) \tag{7}$$

where *n* is the harmonic order; k_n is the *n*th-harmonic wavenumber, with $k_n=nk_1$.

This expression shows that the equivalent surface stress in the x direction depends on the coil geometry, dynamic-current amplitude, static-field strength and magnetostrictive properties of the Fe-Co alloy. The parameters in Table 1 were used to calculate the surface-stress distribution of the proposed transducer.

Table 1 Parameters used in the magnetostrictive patch transducer model.

Parameter	Value	Parameter	Value
Static magnetic-field strength	20×10^4 A/m	Relative permeability of patch, μ_r	11.744
Coil width	5 mm	Electrical conductivity of patch	2.5 MS/m
Wire diameter	0.2 mm	Patch density	8000 kg/m^3
Alternating-current amplitude	5 A	Lift-off distance	0.1 mm
Alternating-current frequency	150 kHz	Patch Lame constant, λ	1.05×10^5 Pa
Vacuum permeability, μ_0	$4\pi\times10^{-7}$ N/A^2	Patch Lame constant, μ	0.76×10^{11} Pa

The solution yields the following relation for Eq.(7):

$$\frac{6\mu\varepsilon_{\bar{H}_z}}{\bar{H}_z}\sum_{n=0}^{\infty}q_n\odot_n\cos\left(k_nx\right)\gg\mu\gamma_{\bar{H}_z}\sum_{n=0}^{\infty}\frac{k_n^2}{q_n}\odot_n\cos\left(k_nx\right) \tag{8}$$

Equation (7) can therefore be simplified to

$$\sigma_x^{(\mathrm{MS,e})}\approx-\frac{6\mu\varepsilon_{\bar{H}_z}}{\bar{H}_z}\sum_{n=0}^{\infty}q_n\odot_n\cos\left(k_nx\right) \tag{9}$$

Equation (9) indicates that the perpendicular-field transducer generates shear-horizontal guided waves through an equivalent surface stress $\sigma_x^{(\mathrm{MS,e})}$ that depends mainly on the Fe-Co alloy's magnetostrictive properties and varies linearly with them.

To validate the analytical model, a two-dimensional finite-element model was developed in COMSOL Multiphysics 6.2 (COMSOL AB, Stockholm, Sweden), as shown in Fig. 2. The geometry and material properties

matched those used in the analytical calculation. The magnetostrictive patch measured 20.0 mm by 0.2 mm, and the air domain measured 30.0 mm by 10.0 mm. The electromagnetic and solid-mechanics fields were coupled through the magnetostriction multiphysics interface, and a background static field was specified in the magnetic-field interface. A locally refined free-triangular mesh was employed, with a maximum element size of approximately 0.025 mm in the magnetostrictive patch; further mesh refinement resulted in a variation of less than 2% in the calculated maximum surface stress, confirming mesh convergence.

A coupled frequency-domain magnetostriction study was performed at 150 kHz, with the prescribed background field used as the static magnetic bias. The magnetic-field domain included the coil, magnetostrictive patch and surrounding air, whereas the solid-mechanics domain was restricted to the patch. The outer air-domain boundaries were assigned the open-field boundary treatment used in the magnetic-field model, and the patch surfaces were mechanically unconstrained. The mesh was locally refined within the 0.2 mm thick patch and near the coil boundaries. Mesh convergence was assessed by further refining these regions and comparing the resulting normalised surface-stress distributions.

The surface stress on the upper face of the magnetostrictive patch was extracted using the COMSOL Multiphysics post-processing tools. Normalised surface stress was sampled along the red dashed line shown in Fig. 2. As shown in Fig. 3, the analytical and finite-element results followed the same trend, with a maximum relative error of 8.71%, supporting the validity of the analytical model.

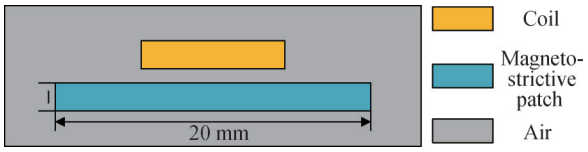


Fig.2 Finite-element model of the magnetostrictive patch transducer.

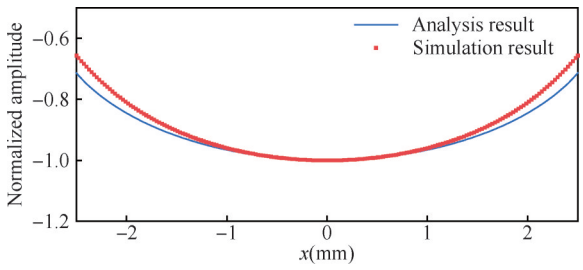


Fig.3 Magnetostrictive surface stresses obtained from the analytical and finite-element models.

A Lorentz-force transduction mechanism may also operate in the proposed transducer. To compare the contributions of the two mechanisms, the equivalent Lorentz-force surface stress was calculated as

$$\tau_x^{(e)} = \frac{i\omega\sigma_e\mu_0\bar{B}I_0}{a}\sum_{n=0}^{\infty}\frac{A_n e^{-k_n h_l}\cos(k_n x)}{q_n\left(k_n + \frac{q_n}{\mu_r}\right)} \quad (10)$$

where $\tau_x^{(e)}$ is the equivalent Lorentz-force surface stress (Pa); $\bar{B}$ is the static magnetic flux density (T); and σ_e is the electrical conductivity (S/m).

The parameters in Table 1 were substituted into Eq. (10), and the resulting stress was compared with that generated by magnetostriction, as shown in Fig. 4. The two mechanisms produced stresses in opposite directions, but the magnetostrictive stress amplitude was substantially greater. The Lorentz-force contribution was therefore small and was neglected. Magnetostriction was the dominant transduction mechanism of the proposed design.

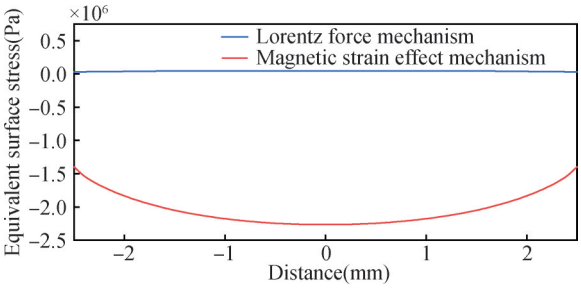


Fig.4 Equivalent surface stresses predicted for the two transduction mechanisms.

3 Results

3.1 Validation of Guided-Wave Excitation by the Proposed Transducer

3.1.1 Experimental Setup

The guided-wave excitation performance was evaluated using the experimental system shown in Fig. 5. The system comprised an RPR-4000 high-power ultrasonic pulser/receiver (RITEC Inc., Warwick, RI, USA), an InfiniiVision DSOX3024T digital storage oscilloscope (Keysight Technologies, Santa Rosa, CA, USA), transmitting and receiving transducers, a magnetostrictive patch, an aluminium plate, and a teslameter. The oscilloscope has a maximum sampling rate of 5 GSa/s.

A 750 mm by 750 mm by 2 mm aluminium plate was used as the test specimen. The transmitting transducer comprised a Fe-Co magnetostrictive patch, a coil and a laboratory-built electromagnet. The 50 mm by 50 mm by 0.1 mm patch was bonded to the plate with epoxy resin. The 10 mm by 10 mm coil contained 50 turns of 0.2 mm diameter enamelled copper wire. The static field at the patch surface was varied by adjusting the electromagnet current and was measured with a teslameter. The receiving transducer was positioned 250 mm from the transmitter.

The evaluation comprised three experiments. First,

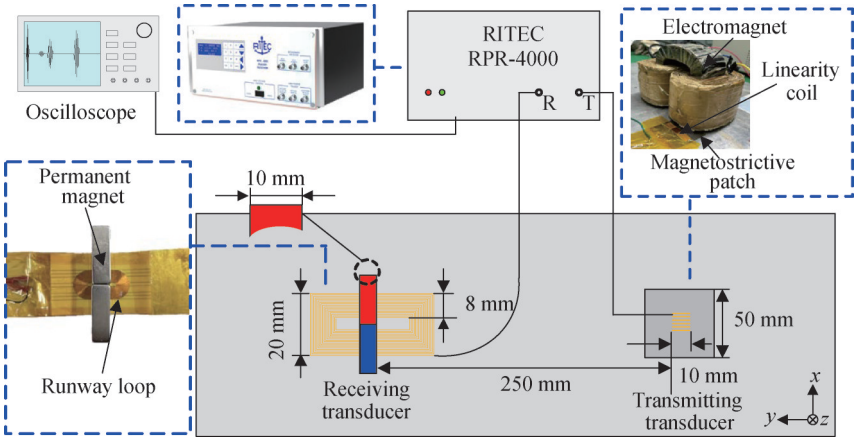


Fig.5 Schematic of the experimental setup for shear-horizontal guided-wave excitation.

the excitation frequency was varied and the guided-wave group velocity was calculated from the time of flight to identify the mode. Second, the transmitter-receiver spacing was varied and a two-dimensional Fourier transform was applied to obtain the frequency-wavenumber distribution and further verify the mode content. Finally, the perpendicular static-field strength was varied and the signal amplitude was recorded. The result was compared with the excitation performance of other magnetostrictive patch transducer configurations.

3.1.2 Guided-Wave Excitation Results and Performance Analysis

Guided-wave mode-identification experiments were conducted on the aluminium plate to determine the modes excited by the proposed transducer. The excitation frequency was varied, and group velocity was calculated from the measured time of flight. Fig. 6 compares the theoretical dispersion curves of the shear-horizontal modes with the measured group velocities.

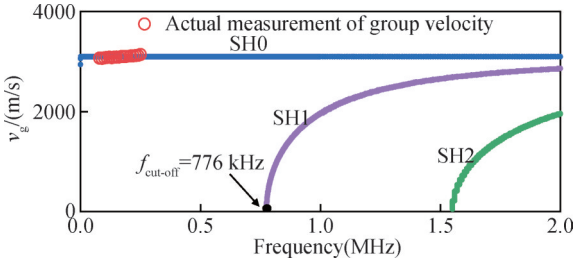


Fig.6 Theoretical dispersion curves of shear-horizontal guided waves and measured group velocities.

As shown in Fig. 6, the measured group velocity was approximately 3100 m/s and remained nearly constant with frequency. This value agrees with the theoretical velocity of the fundamental shear-horizontal mode in the specimen, confirming that the transducer effectively generated the non-dispersive fundamental mode over the test frequency range.

The excitation frequencies were then set to 100 and 200 kHz. The transmitter-receiver spacing was increased from 250 to 330 mm in 2 mm increments, and guided-wave signals were recorded at each position. Two-dimensional Fourier transformation produced the frequency-wavenumber distributions shown in Fig. 7.

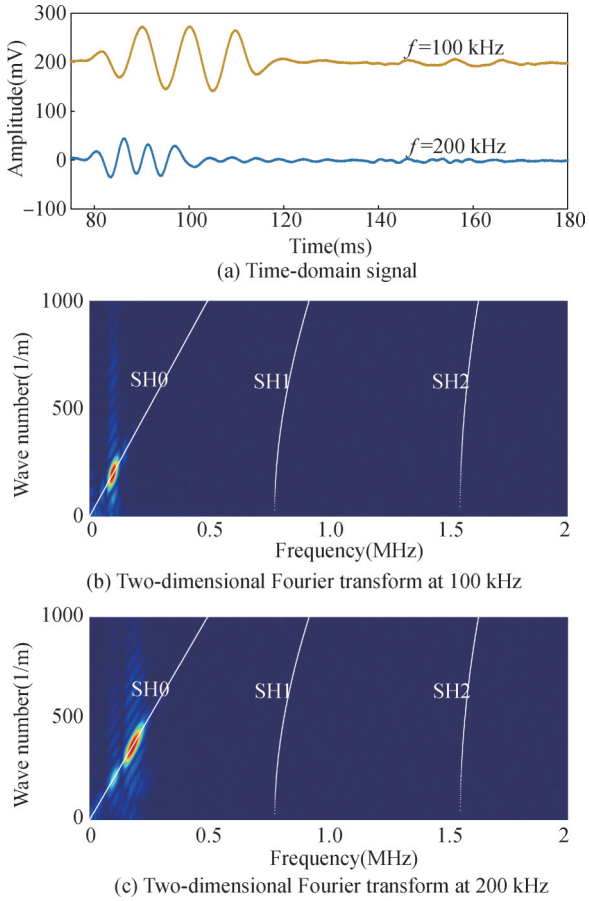


Fig.7 Signals received at excitation frequencies of 100 and 200 kHz.

The energy in the frequency-wavenumber maps was concentrated near the dispersion curve of the fundamental shear-horizontal mode. Thus, when the excitation frequency was below the cut-off frequency of the first higher-order mode, the proposed transducer generated a relatively pure fundamental mode.

To examine the effect of static-field strength on guided-wave excitation, the electromagnet current was varied incrementally. The perpendicular static magnetic flux density at the patch surface and the amplitude of the received signal were recorded, as shown in Fig. 8.

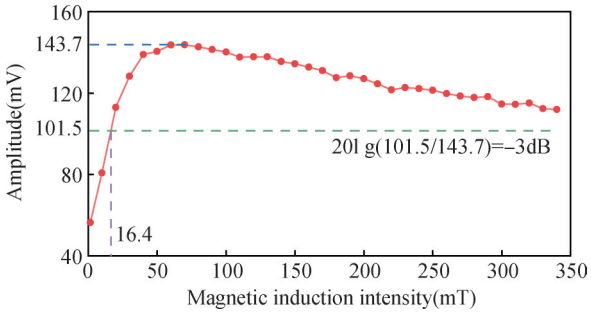


Fig.8 Guided-wave amplitude as a function of perpendicular static magnetic flux density.

The guided-wave amplitude first increased and then decreased as the perpendicular static magnetic flux density at the patch surface increased. The maximum amplitude of 143.7 mV occurred at approximately 70.0 mT. According to the -3 dB criterion, the amplitude exceeded 101.5 mV when the flux density was above 16.4 mT, indicating effective excitation over a broad static-field range.

The proposed design was compared with three alternatives under identical experimental conditions: a horizontal-field transducer based on the inverse Wiedemann effect, a horizontal-field transducer based on the Wiedemann effect and a premagnetised transducer. Figure 9 shows the four configurations, and Fig. 10 compares their mean guided-wave amplitudes. To evaluate the repeatability of the guided-wave excitation measurements, 40 independent signals were acquired for each transducer configuration under the same excitation conditions. The transducer position and the measurement location on specimens of the same material were changed between measurements. The mean amplitudes and corresponding standard errors were calculated from the 40 measured signals. The standard error (SE) was calculated using Eq. (11):

$$SE = \frac{s}{\sqrt{n-1}} \tag{11}$$

where s is the sample standard deviation and n is the number of measurements.

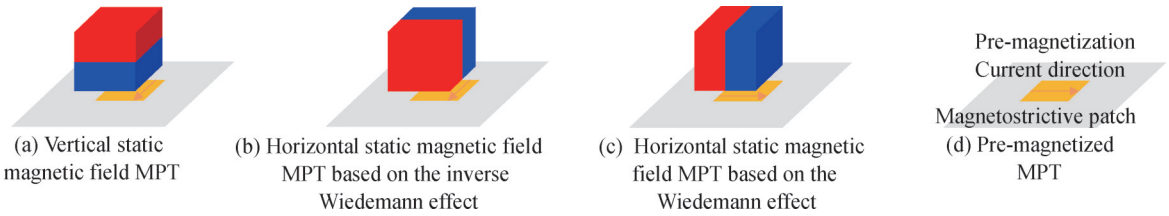


Fig.9 Configurations of the magnetostrictive patch transducers used for comparison.

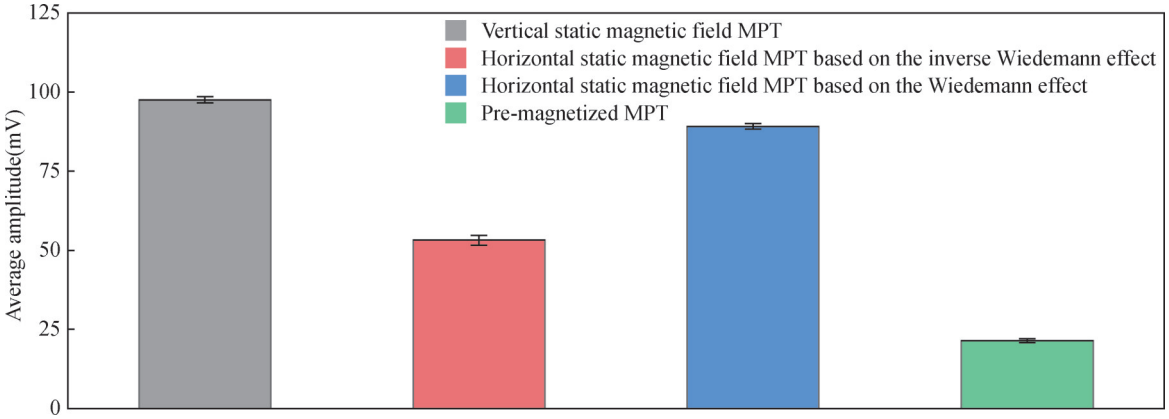


Fig.10 Mean amplitudes of the guided waves generated by the different transducers.

The mean shear-horizontal guided-wave amplitude generated by the proposed transducer was similar to that of the horizontal-field design based on the Wiedemann effect and approximately twice that of the inverse-Wiedemann-effect design. The small standard errors indicate stable guided-wave excitation under repeated positioning and measurement conditions. Its compact magnetic circuit also facilitates array deployment.

3.2 Experimental Validation of Full-Waveform Inversion Imaging

3.2.1 Full-Waveform Inversion Method

Full-waveform inversion was applied to the experimental signals to evaluate the proposed transducer for defect imaging. The method estimates model parameters $\boldsymbol{m}$ by minimising the mismatch between

observed data $\boldsymbol{d}_{\text{obs}}$ and simulated data $\boldsymbol{d}_{\text{cal}}$. The data residual $\Delta\boldsymbol{d} = \boldsymbol{d}_{\text{obs}} - \boldsymbol{d}_{\text{cal}}$ is minimised through the objective function $\Phi(\boldsymbol{m})$, expressed as:

$$\min_{m} \Phi(\boldsymbol{m}) = \frac{1}{2} \| \Delta\boldsymbol{d} \|^2 = \frac{1}{2} \left(\Delta\boldsymbol{d}^T \right)^* \Delta\boldsymbol{d} \tag{12}$$

where * denotes complex conjugation, ensuring that the objective function $\Phi(\boldsymbol{m})$ is real valued.

Full-waveform inversion minimises an objective function. Starting from the initial model $\boldsymbol{m}_0$, the model at iteration k is updated as:

$$\boldsymbol{m}_{k+1} = \boldsymbol{m}_k + \Delta\boldsymbol{m}_k = \boldsymbol{m}_k + \boldsymbol{a}_k \boldsymbol{p}_k \tag{13}$$

where $\Delta\boldsymbol{m}_k$ is the model update; $\boldsymbol{a}_k$ is the step length; and $\boldsymbol{p}_k$ is the search direction.

The time-domain finite-element simulation and the forward model used by the frequency-domain inversion introduce a modelling discrepancy. A calibration factor derived from a defect-free specimen was therefore used to improve consistency between the experimental data and the inversion model. It is defined as

$$Q = \frac{\text{FFT}(d_{\text{cal},0})}{\text{FFT}(d_{\text{obs},0})} \tag{14}$$

Minimum remaining thickness is an important indicator of structural integrity. The metric e_{depth} was therefore used to quantify the maximum depth error of the reconstructed defect, as defined in Ref. [23]:

$$e_{\text{depth}} = \frac{d_{\min} - d^*_{\min}}{d_0} \tag{15}$$

where $d_{\min}$ is the minimum thickness of the actual defect, $d^*_{\min}$ is the minimum thickness of the reconstructed defect, and d_0 is the original specimen thickness.

The inversion was initialized using a homogeneous defect-free model with a background wave velocity of 3000 m/s. The frequency-domain forward model was discretized on a uniform spatial grid and surrounded by a 15 mm perfectly matched layer to suppress artificial boundary reflections. For the dual-row transmit–dual-row receive configuration, 32 measurement positions were arranged in two rows, with 16 positions in each row. Sequential transmission and reception produced a 32 × 32 dataset.

The search direction was determined using the limited-memory Broyden-Fletcher-Goldfarb-Shanno algorithm. Unlike the Newton method, the L-BFGS algorithm does not explicitly calculate or store the complete Hessian matrix. Instead, it uses a limited number of previous model and gradient updates to approximate the inverse Hessian matrix, thereby reducing the memory requirement for large-scale inversion. The full-waveform inversion and L-BFGS-B optimisation were implemented in MATLAB R2024a (MathWorks, Natick, MA, USA).

For the numerical evaluations of array configuration and defect geometry, the maximum number of iterations was set to 80. The inversion was terminated when the relative error was below 10^{-5} or when the maximum number of iterations was reached.

3.2.2 Experimental Validation on Plates and Pipes

Time-domain finite-element models were established in COMSOL Multiphysics to generate guided-wave signals for the subsequent full-waveform inversion. The simulated time-domain signals were windowed and transformed into the frequency domain before being used as the observed data in the inversion.

Five array configurations were evaluated using a 150 mm × 150 mm model containing a 30-mm-diameter circular defect. The background and defect wave velocities were 3000 and 2500 m/s, respectively. As shown in Fig. 11(a–e), the circular array and the dual-row transmit–dual-row receive array provided more complete reconstructions, whereas the limited-view configurations exhibited incomplete or distorted defect contours. The dual-row transmit – dual-row receive array was therefore selected for subsequent analyses. The maximum iteration number was 80, and the errors became approximately stable after 60 iterations, as shown in Fig. 11(i).

Using the selected array, a 30 mm × 30 mm rectangular defect, a 30 mm × 2 mm crack-like defect and a 30-mm-diameter conical wall-thinning defect were further investigated. The rectangular and crack-like defects had a wave velocity of 2500 m/s, whereas the conical-defect velocity gradually decreased from 3000 m/s at the boundary to 2500 m/s at the centre. As shown in Fig. 11(f – h), the rectangular defect contour was clearly reconstructed, the narrow crack-like region remained identifiable, and the gradual velocity variation of the conical defect was recovered. These results demonstrate that the inversion method can accommodate both abrupt and continuously varying defect profiles under the finite-element conditions considered.

3.2.3 Experimental Validation on Plates and Pipes

Plate and pipe experiments were conducted to further evaluate the combined transducer and inversion method. The plate tests assessed contour reconstruction in a regular planar structure, whereas the pipe tests examined feasibility for a curved structure. A defect-free specimen provided the calibration data in each test, and rectangular and circular defects were imaged.

Three aluminium plates, each measuring 1000 mm by 1000 mm by 10 mm, were used. The first plate was defect free and provided calibration data. A rectangular defect was machined at the centre of the second plate, and a circular defect was machined at the centre of the third. Their positions and dimensions are shown in Fig. 12.

The pipe tests used three aluminium pipes with an outer diameter of 200 mm, a length of 1000 mm and a wall thickness of 10 mm. The first pipe was defect free and provided calibration data. The second contained a central rectangular defect measuring 80 mm by 56 mm, and the third contained a central circular defect with a radius of 28 mm. These features represented local wall thinning or corrosion. Their

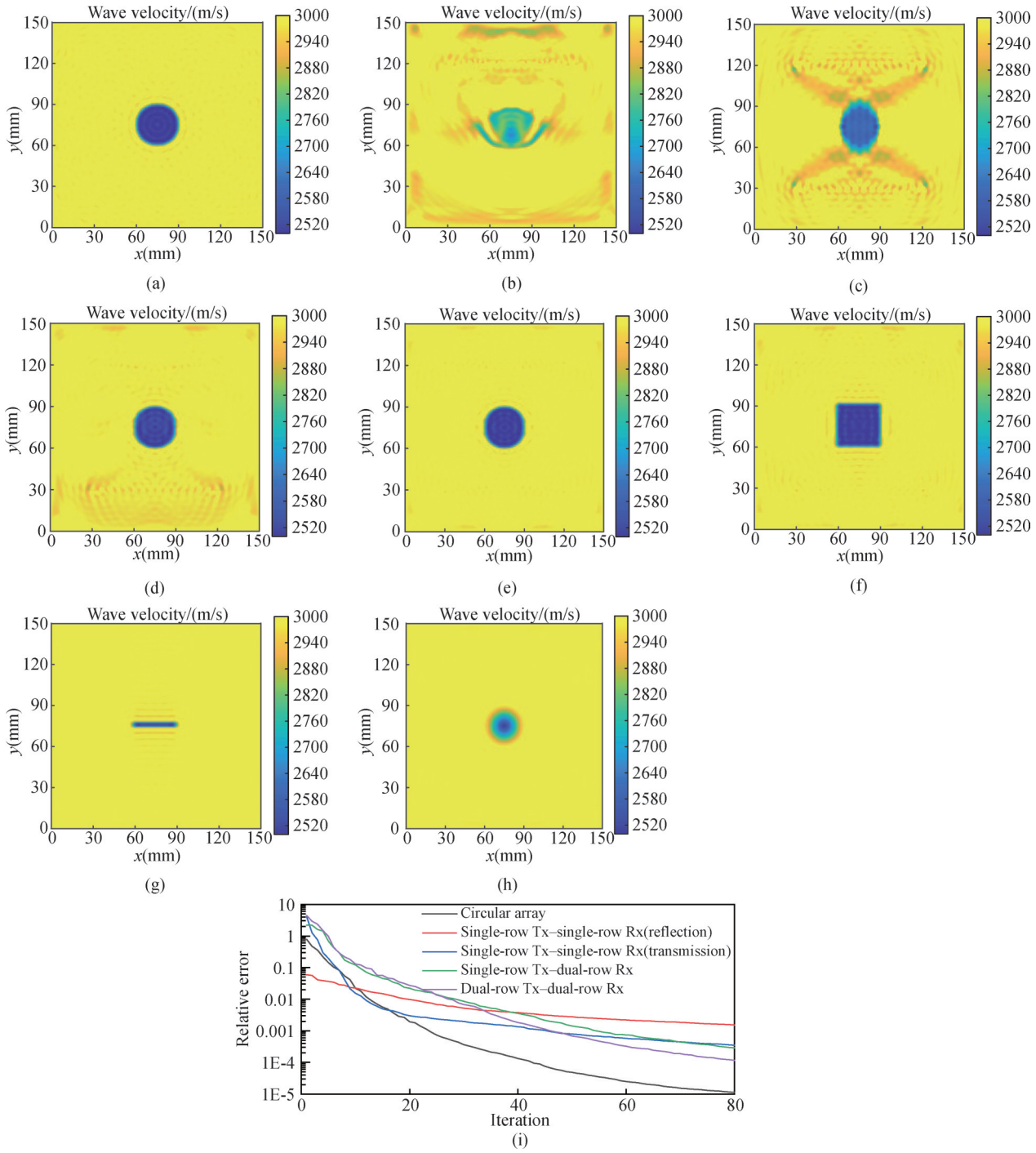


Fig.11 Full-waveform inversion results based on COMSOL finite-element data: (a-e) reconstruction results obtained using five array configurations; (f-h) reconstruction results for rectangular, crack-like and conical wall-thinning defects; and (i) corresponding convergence histories.

dimensions are shown in Fig. 13.

The plate and pipe specimens used for imaging both had a wall thickness of 10 mm. Unlike the SH0 mode used to verify the fundamental guided-wave excitation performance on the 2-mm-thick plate, the first higher-order shear-horizontal mode was selected for defect imaging because of its greater sensitivity to wall-thickness variation. At an excitation frequency of 300 kHz, the frequency – thickness product of the imaging specimens was 3.0 MHz·mm, allowing the SH1 mode to propagate. Its dispersive characteristics result in measurable changes in phase velocity and waveform as the local thickness varies, thereby providing additional information for full-waveform inversion. Accordingly, a three-cycle, 300-kHz tone burst was used to excite the SH1 mode. The array transducers sequentially transmitted and received signals to produce a 32 × 32 experimental dataset. A rectangular window was then applied to isolate the selected SH1 wave packet and reduce interference from other modes before inversion.

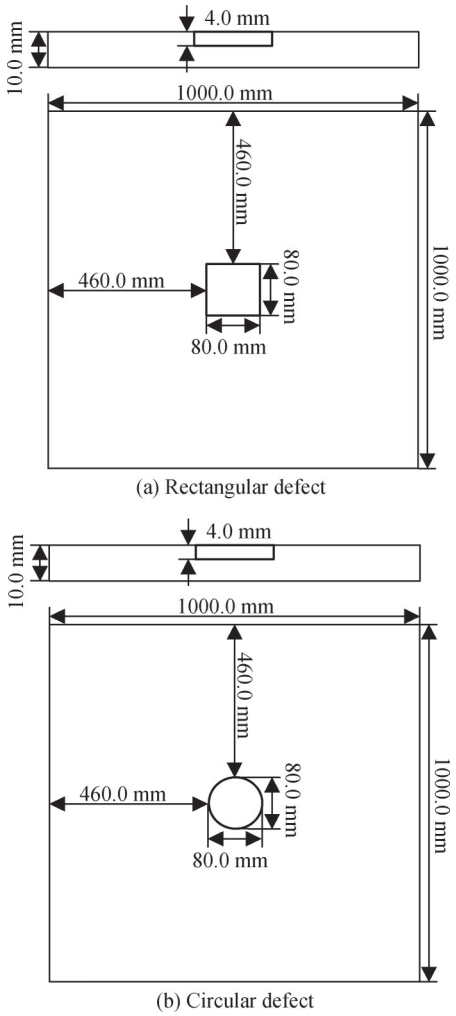


Fig.12 Locations and dimensions of the plate defects.

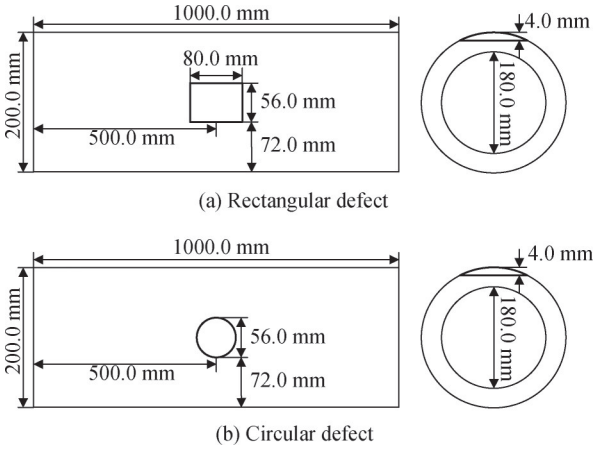


Fig.13 Geometry of the pipe defects.

After the guided-wave excitation performance had been validated, full-waveform inversion was applied to the plate defects. The rectangular and circular defects were imaged separately. The measured time-domain signals were windowed, transformed by the fast Fourier transform and calibrated before being supplied to the inversion algorithm. The resulting thickness distributions are shown in Fig. 14.

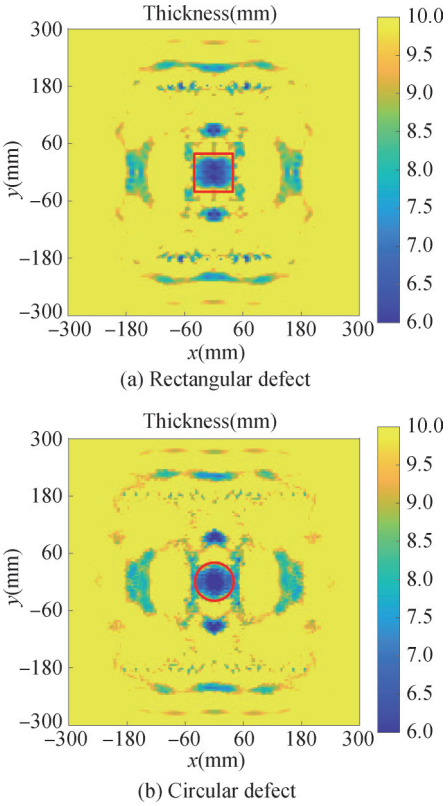


Fig.14 Full-waveform inversion images of the plate defects.

Both the circular and rectangular defect contours were clearly reconstructed. Figure 15 compares the reconstructed and actual contours, which showed good overall agreement.

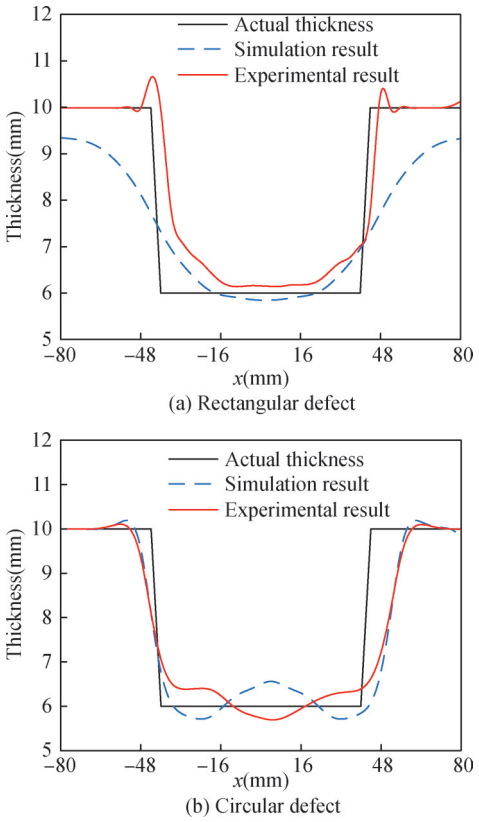


Fig.15 Reconstructed and actual contours of the plate defects.

The maximum depth error was -1.4% for the rectangular plate defect and 3.4% for the circular defect. Both values were within 5.0%, indicating that the inversion method recovered the plate-defect contours and estimated their depths with good accuracy.

Full-waveform inversion was also applied to the pipe defects to evaluate the proposed transducer on a curved structure. The imaging results are shown in Fig. 16, and Fig. 17 compares the reconstructed and actual defect contours.

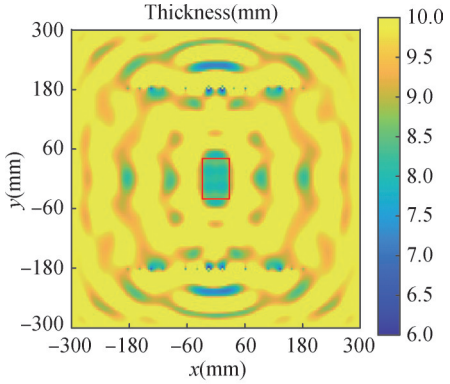


Fig.16 Full-waveform inversion images of the pipe defects.

The inversion recovered the overall wall-thinning pattern, although deviations remained near the defect boundaries and at the maximum-depth locations. The maximum depth error was -12.8% for the rectangular defect and -11.9% for the circular defect. These errors were greater than those obtained for the plates, but the principal locations and contours remained identifiable. The results support the feasibility of using an array of the proposed transducers for pipe-defect imaging.

4 Discussion

This study examined the guided-wave excitation performance of a magnetostrictive patch transducer with a perpendicular static magnetic field and its application to full-waveform inversion imaging. In contrast to a conventional horizontal-field design, the proposed configuration directs the static bias field through the patch thickness. The magnetising face therefore acts more

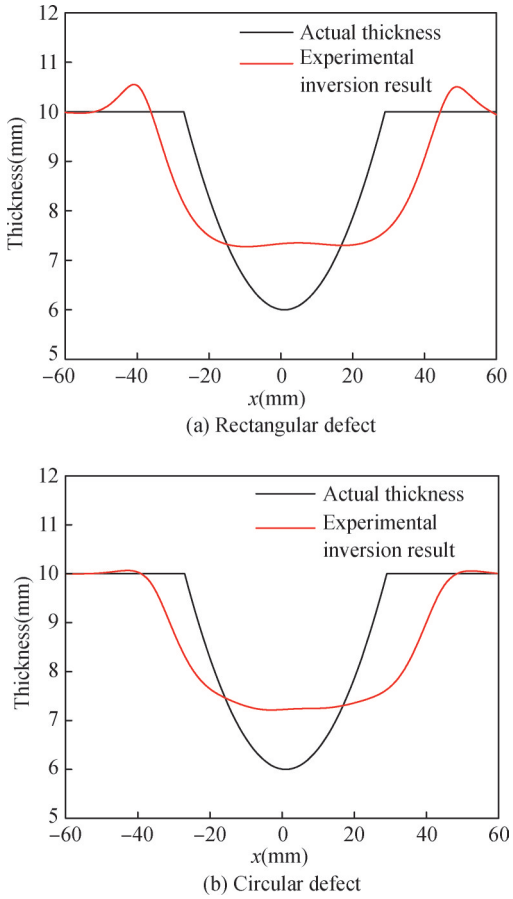


Fig.17 Reconstructed and actual contours of the pipe defects.

directly on the transduction region. This arrangement reduces the field attenuation and non-uniformity associated with increased magnet spacing in horizontal-field designs. Its compact geometry and flexible array layout are particularly advantageous for large plates and curved structures.

The perpendicular static field and the dynamic field generated by the coil act jointly on the Fe-Co patch, producing an equivalent surface stress that excites shear-horizontal guided waves. The analytical and finite-element results showed that the magnetostrictive stress was substantially greater than the Lorentz-force stress. Magnetostriction was therefore the dominant transduction mechanism. Experimentally, guided-wave amplitude first increased and then decreased with static-field strength, consistent with the magnetostrictive response of the Fe-Co alloy. At low field strength, insufficient domain alignment limits the response. Greater field strength improves domain alignment and increases the guided-wave amplitude. As magnetic saturation is approached, however, the incremental response to the dynamic field decreases and the signal weakens. The maximum amplitude occurred at approximately 70 mT.

Full-waveform inversion requires guided-wave signals with sufficient amplitude, signal-to-noise ratio, mode purity and phase stability. Mode identification, static-field optimisation and comparisons among transducer configurations showed that the proposed

design provided suitable signals for inversion. For the plates, the rectangular and circular defect contours were clearly reconstructed, with maximum depth errors of -1.4% and 3.4%, respectively. The corresponding errors increased to -12.8% and -11.9% for the pipe defects, mainly because structural curvature, circumferential propagation, limited array sampling and boundary reflections increased the discrepancy between the forward model and the experimental wavefield.

The present study has several limitations. First, the experimental validation was conducted using rectangular and circular wall-thinning defects, whereas the crack-like and conical wall-thinning defects were evaluated using COMSOL finite-element data. Therefore, the demonstrated adaptability to different defect geometries should be interpreted within the numerical and experimental conditions considered in this study. Second, reconstruction quality remains dependent on array coverage and the consistency between the forward model and the measured guided-wave field. This dependence is more evident for pipe specimens because structural curvature, circumferential propagation and boundary reflections introduce additional modelling discrepancies.

The computational cost is mainly associated with repeated forward-wavefield solutions and gradient calculations. In the present analyses, the maximum number of iterations was 80, the relative-error threshold was 10^{-5}, and the inversion errors became approximately stable after 60 iterations. Because absolute reconstruction time is affected by the hardware platform, linear solver, parallelisation strategy and code implementation, computational performance was characterised using the optimisation method, iteration number, convergence criterion and convergence history. Future work will focus on improving the forward model for curved structures, optimising array layout and frequency selection, extending the evaluation to broader measurement and operating conditions, and introducing parallel or graphics-processing-unit-based acceleration.

5 Conclusion

A magnetostrictive patch transducer with a perpendicular static magnetic field was developed and combined with full-waveform inversion for guided-wave imaging of defects in plates and pipes. The main findings are as follows.

(1) An analytical equivalent surface-stress model was established for the transducer and validated by finite-element analysis. The analytical and numerical stress distributions showed consistent trends, and magnetostriction was identified as the dominant transduction mechanism.

(2) The transducer effectively generated shear-horizontal guided waves. Signal amplitude was greatest at a surface magnetic flux density of approximately 70 mT and was about twice that of a horizontal-field design based on the inverse Wiedemann effect.

(3) COMSOL finite-element analyses showed that the dual-row transmit – dual-row receive array provided favourable reconstruction among the investigated configurations. Rectangular, crack-like and conical wall-thinning defects were subsequently reconstructed using finite-element guided-wave data. Experimental signals further enabled full-waveform inversion of rectangular and circular wall-thinning defects in plates and pipes, with maximum depth errors of -1.4% and 3.4% for the plate defects and -12.8% and -11.9% for the pipe defects.

Author Contributions:

Conceptualization: S. W. and Z. L.; Methodology: J. W., S. W., and Z. L.; Software: J. W.; Validation: J. W.; Formal analysis: J. W.; Investigation: J. W.; Resources: S. W. and Z. L.; Data curation: J. W.; Visualization: J. W.; Writing—original draft: J. W.; Writing—review and editing: S. W. and Z. L.; Supervision: S. W. and Z. L.; Project administration: S. W. and Z. L. All authors have read and agreed to the published version of the manuscript.

Acknowledgments:

The authors would like to thank the laboratory members for their assistance in experimental testing, data acquisition, and technical discussions during this study.

Funding Information:

This research received no external funding.

Data Availability:

The main data supporting the findings of this study are available within the paper.

Conflicts of Interest:

The authors declare no competing interests.

Use of Generative AI and AI-Assisted Technologies

No generative AI was used.

References

[1] Chen Y H, Li L J, Li D D, et al. External corrosion mechanisms of buried metallic pipelines in oilfields [J]. *Corrosion & Protection,* **2015**, 36(11): 1009-1013. (in Chinese)

[2] Li H Q, Wang X. Approaches to improving the quality of natural-gas pipeline transportation [J]. *Cleaning World,* **2022**, 38(8): 67-69. (in Chinese)

[3] Zhang B X, Zhang P, Yan S G, et al. Advances in ultrasonic imaging inspection [J]. *Journal of Shaanxi Normal University (Natural Science Edition),* **2022**, 50(6): 1-16. (in Chinese)

[4] Sun Z, Rocha B, Wu K T, et al. A methodological review of piezoelectric-based acoustic-wave generation and detection techniques for structural health monitoring [J]. *International Journal of Aerospace Engineering,* **2013**, 2013: 1-22.

[5] Wu R, Shi W Z, Lu C, et al. Quantitative electromagnetic ultrasonic inspection of shear-horizontal guided waves in aerospace stainless-steel sheets [J]. *Acta Aeronautica et Astronautica Sinica,* **2022**, 43(9): 735-748. (in Chinese)

[6] Zhu K. Broadband high-sensitivity ultrasonic transducers based on an acoustic-impedance gradient matching layer [D]. Harbin Institute of Technology, **2025**. (in Chinese)

[7] Zang X, Xu Z D, Lu H, et al. Ultrasonic guided-wave techniques and applications in pipeline defect detection: a review [J]. *International Journal of Pressure Vessels and Piping,* **2023**, 206: 105033.

[8] Lee J H, Lee S J. Application of laser-generated guided waves for evaluation of corrosion in carbon-steel pipe [J]. *NDT & E International,* **2009**, 42(3): 222-227.

[9] He C F, Zheng M F, Lu Y, et al. Development, applications and challenges of ultrasonic guided-wave testing [J]. *Chinese Journal of Scientific Instrument,* **2016**, 37(8): 1713-1735. (in Chinese)

[10] Panda A K, Sharan P K, Roy R K, et al. Generation and detection of guided waves in a defective pipe using rapidly quenched magnetostrictive ribbons [J]. *Smart Materials and Structures,* **2012**, 21(4): 045015.

[11] Cho S H, Han S W, Park C I, et al. High-frequency torsional modal testing of a long cylinder by magnetostriction [J]. *Applied Physics Letters,* **2007**, 91(7): 071908.

[12] Long S R, Zhong Y N, Liu Y, et al. Effect of bias-field uniformity on the output characteristics of a magnetostrictive guided-wave sensor [J]. *Acta Petrolei Sinica,* **2014**, 35(2): 390-394. (in Chinese)

[13] Seung H M, Kim Y Y. Generation of omnidirectional shear-horizontal waves in a ferromagnetic plate by a magnetostrictive patch transducer [J]. *NDT & E International,* **2016**, 80: 6-14.

[14] Zhang F, Ma G L, Li C, et al. Design of a torsional guided-wave transducer for pipe monitoring based on the inverse Wiedemann effect [J]. *Instrument Technique and Sensor,* **2022** (7): 28-33. (in Chinese)

[15] Ng K, Tse P W. Design of a remote and integrated Sagnac interferometer that can generate narrowband guided waves using lasers and effective optics to detect defects in plates [J]. *Optics & Laser Technology,* **2020**, 123: 105923.

[16] Miao H, Li F. Shear-horizontal wave transducers for structural health monitoring and non-destructive testing: a review [J]. *Ultrasonics,* **2021**, 114: 106355.

[17] Nurmalia, Nakamura N, Ogi H, et al. Mode-conversion behaviour of shear-horizontal guided waves in a tapered plate [J]. *NDT & E International,* **2012**, 45(1): 156-161.

[18] Watkins R, Jha R. A modified time-reversal method for Lamb-wave-based diagnostics of composite structures [J]. *Mechanical Systems and Signal Processing,* **2012**, 31: 345-354.

[19] Liu Z, Yu H, Fan J, et al. Baseline-free delamination inspection in composite plates by combining non-contact air-coupled Lamb-wave scanning with a virtual time-reversal algorithm[J]. *Smart Materials and Structures,* **2015**, 24(4): 045014.

[20] Hormati A, Jovanovic I, Roy O, et al. Robust ultrasound travel-time tomography using the bent-ray model [C] // D'hooge J, McAleavey S A. SPIE Medical Imaging. San Diego, CA, USA, **2010**: 76290I.

[21] Malyarenko E V, Hinders M K. Ultrasonic Lamb-wave diffraction tomography [J]. *Ultrasonics,* **2001**, 39(4): 269-281.

[22] Rao J, Ratassepp M, Fan Z. Guided-wave tomography based on full-waveform inversion [J]. *IEEE Transactions on Ultrasonics,* Ferroelectrics, and Frequency Control, **2016**, 63 (5): 737 – 745.

[23] Rao J, Ratassepp M, Fan Z. Limited-view ultrasonic guided-wave tomography using an adaptive regularisation method [J]. *Journal of Applied Physics,* **2016**, 120(19): 194902.

[24] Rao J, Ratassepp M, Fan Z. Investigation of the reconstruction accuracy of guided-wave tomography using full-waveform inversion [J]. *Journal of Sound and Vibration,* **2017**, 400: 317-328.

[25] Rao J, Yang J, Ratassepp M, et al. Multiparameter reconstruction of velocity and density using ultrasonic tomography based on full-waveform inversion [J]. *Ultrasonics,* **2020**, 101: 106004.

[26] Rao J, Ratassepp M, Lisevych D, et al. Online corrosion monitoring of plate structures based on guided-wave tomography using piezoelectric sensors [J]. *Sensors,* **2017**, 17 (12): 2882.

[27] Lin M, Smith C, Rao J, et al. A regularisation technique for quantitative imaging of corrosion in pipelines [C] // 46th Annual Review of Progress in Quantitative Nondestructive Evaluation (QNDE 2019). Portland, OR, USA, 2019.

[28] He J, Rao J, Fleming J D, et al. Numerical ultrasonic full-waveform inversion for complex structures in coupled two-dimensional solid-fluid media [J]. *Smart Materials and Structures,* **2021**, 30(8): 085044.

[29] Rao J, Sing S L, Lim J C W, et al. Detection and characterisation of defects in directed-energy-deposited multimaterial components using full-waveform inversion and reverse-time migration [J]. *Virtual and Physical Prototyping,* **2022**, 17(4): 1047-1057.

[30] Ratassepp M, Rao J, Yu X, et al. Modelling the effect of anisotropy in ultrasonic guided-wave tomography [J]. *IEEE Transactions on Ultrasonics, Ferroelectrics, and Frequency Control,* **2022**, 69(1): 330-339.